Article

Density Functional Theory Study of NiFeCo Trinary Oxy-Hydroxides for an Efficient and Stable Oxygen Evolution Reaction Catalyst

Habib Ullah, Adeline Loh, David P. Trudgeon, and Xiaohong Li*

Read Online

ACCESS | Metrics & More | Article Recommendations | Supporting Information

ABSTRACT: NiOOH and its doped species are widely used as electrocatalysts for the oxygen evolution reaction (OER) in alkaline media. In this work, we carried out comprehensive density functional theory (DFT) simulations of Ni-based electrocatalysts for the OER by applying suitable dopants in β-NiOOH. A range of Fe and Co atoms (%) are employed as doping agents to increase the overall catalytic ability, stability, and feasibility of NiOOH. Our simulations indicate that $Ni_{88\%}Fe_{6\%}Co_{6\%}OOH$ is efficient, stable, and provides more catalytic sites at the surface of resulting catalysts for water adsorption and dissociation, which facilitate the OER. The lower overpotential for the OER is estimated from the higher adsorption energy of water molecule over the surface of $Ni_{88\%}Fe_{6\%}Co_{6\%}OOH$, followed by other electronic properties such as band structure, electrostatic potential, the density of states, and surface formation energy.
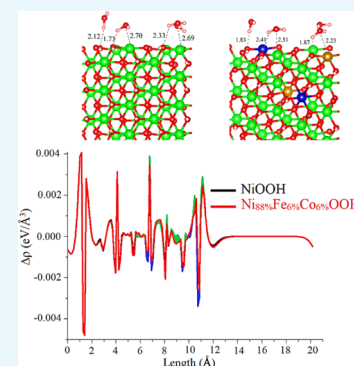
1. INTRODUCTION

Electrochemical water splitting is a combination of two half-reactions, where the oxygen evolution reaction (OER) occurs at the anode and hydrogen evolution reaction (HER) at the cathode.[1,2] Of the two half-reactions, the OER requires four-electron transfers per oxygen molecule, which makes it more complex compared to HER where a two-electron transfer is required and subsequently reduces the efficiency of electrolyzer devices.[3−5] At present, the proton exchange membrane (PEM) electrolyzer, operated in acidic media, is quite successful, and commonly Ir- and Ru-based catalysts have high activity and stability for the OER.[6,7] However, these catalyst materials and proton exchange membranes are very expensive and can be an obstacle to the large-scale hydrogen production. To avoid this dependency on expensive and precious metal catalysts and membranes, efficient and low-cost OER catalysts need to be developed. A wide range of catalyst materials can work in alkaline media, especially the first-row transition metal oxides that have shown promising activity for the OER.[3−5,8,9]

The interest in the nickel hydroxide and nickel oxyhydroxide $(Ni(OH)_2/NiOOH)$ redox couple dates back to the first decade of the 20th century, where $Ni(OH)_2/NiOOH$ was used as cathodes for alkaline batteries such as Ni−Cd, Ni−Fe, Ni−Zn, and Ni−MH batteries.[10,11] To reduce the overpotential of the OER, various groups have reported using the mixed nickel oxides, where Fe, Cr, Co, Ce, and Mo are employed as doping agents.[12−16] In these reports, nickel-based materials have been proved as efficient and stable catalysts for the OER in alkaline media, the overpotentials of the OER of mixed nickel oxides are reduced by a factor of up to ∼100 to 200 mV.[12−14]

Prior to the design and development of new electrocatalysts with desirable performance, it is important to understand the structural and electronic properties of catalyst materials. Nickel oxide and hydroxide exist in different polymorphs such as alpha, beta, and gamma $Ni(OH)_2/NiOOH$, as shown in Scheme 1.[17] Bode et al. demonstrated the redox reaction between the different polymorphs of $Ni(OH)_2−Ni(II)/NiOOH−Ni(III)$.[17] The $\alpha−\gamma$ transformation may involve more than one electron transfer per Ni atom (up to 1.6−1.67 electrons) due to the nonintegral average oxidation states of the α and γ phases that occur because of the presence of anions (e.g., NO_3^-, CO_3^{2-}, SO_4^{2-}, Cl^-, etc.) and cations (e.g., Li^+, Na^+, K^+, etc.) in the water layers in α-$Ni(OH)_2$ and γ-NiOOH, respectively.[18,19] Among all of these polymorphs, β-$Ni(OH)_2$ and β-NiOOH are the most active and stable species for the OER.[18−26] On the other hand, γ-NiOOH and α-$Ni(OH)_2$ are highly efficient but unstable due to large interlamellar space as a result of the insertion of an extra layer of water and cations or anions between the two Ni-containing sheets (see the modeling in Scheme 1).[19] In addition, α-$Ni(OH)_2$ was found to be unstable and will convert to β-$Ni(OH)_2$ through a slow aging process.[19]

In the present work, a reduced β-$Ni(OH)_2$ and its oxidized β-NiOOH are selected as parent material for the development
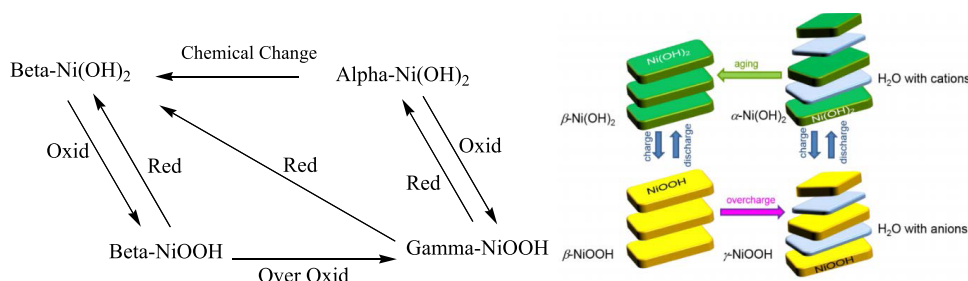
Scheme 1. Schematic (Left) and Modeling (Right) Representation of Bode's Diagram for Ni(OH)₂−NiOOH Redox Transformations[19]

of the proposed catalysts. We computationally investigate a feasible and efficient termination of β-NiOOH, followed by appropriate doping with Fe and Co, to reduce the oxygen overpotential and thus improve the OER efficiency. Solid-state density functional theory (DFT) is employed for the computational simulations. The lower overpotential for the OER is estimated from the higher adsorption energy of water molecule over the surface of the catalyst, followed by other electronic properties such as band structure, electrostatic potential, density of states, and surface formation energy.

2. RESULTS AND DISCUSSION

2.1. Selection of an Appropriate Slab and Water Interaction. Geometries of the unit cell, supercell, and slabs are optimized prior to their electronic properties' simulations. The optimized crystal structure of the unit cell is compared with the available crystallographic parameters of β-NiOOH.[20] As discussed in our previous reports,[21,22] Perdew−Burke−Ernzerhof/generalized gradient approximation (PBE/GGA) accurately reproduces the experimental geometric data. In addition, the per-atom cohesive formation energy of Ni, Fe, Co, and O are simulated to validate our computational method (see Table S1).

The simulated cohesive formation energy of Ni is 5.88 eV/atom at GGA/PBE, using HGH pseudopotential with a tier 4 basis set, which is comparable with the experimentally reported value (4.44 eV/atom).[23] In addition, the calculated cohesive formation energy of other atoms such as Fe, Co, and O are 6.80, 5.56, and 3.7 eV/atom, while their experimental values are 4.28, 4.39, and 2.60 eV/atom, respectively.[23] The difference between theoretical and experimental cohesive formation energy is due to the choice of basis set in ab initio simulations. For the selection of an appropriate slab (model), the formation energy and electrostatic potential of these four different slabs are calculated and listed in Table S2. Comparative analysis of the data in Table S2 shows that NiOOH along the [010] plane is the most stable with the highest surface formation energy of 0.60 eV/Å² as compared to the other phases of NiOOH. This has therefore been selected as the parent species for Fe and Co doping (vide infra). In addition, all of these surfaces are constructed without any dipole. The surface formation energy of these slabs, E_{surf}, was calculated with the help of the eq 1

$$E_{surf} = \frac{1}{2A}(E_{slab} - NE_{bulk}) \qquad (1)$$

where E_{slab} is the total energy of the slab, E_{bulk} is the energy per atom of the bulk, N denotes the number of atoms in the surface slab, and A is the cross-sectional area of the surface slab unit cell.[24−26]

The electrostatic potential map of NiOOH (010) and its water interacted species are given in Figure 1, where the
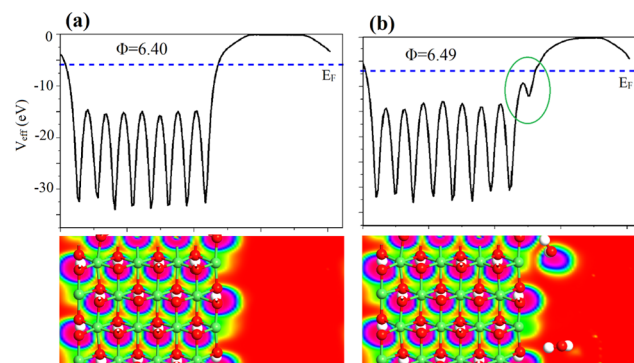

Figure 1. Electrostatic potential map of NiOOH (a) and NiOOH@H₂O (b) along the Z-direction.

electrostatic potentials in the vacuum level are zero that further confirms their stability. Upon interaction with water molecules, a slight increase in the work function (Φ) demonstrates good interaction between the catalyst (NiOOH) and water molecules.

To investigate the catalytic activity, water molecules interact at the surface of our proposed catalyst (NiOOH). As discussed earlier, the most stable phase of NiOOH along [010] is chosen as a model catalyst for Fe and Co dopants, followed by interaction with water molecules. Four water molecules are placed on the surface of NiOOH(010), at an appropriate distance, and the system was allowed to be relaxed, using the mentioned method (vide supra). Hereafter, the NiOOH(010) will be represented as NiOOH. All of the four water molecules are strongly adsorbed over the surface of NiOOH with an average interbond distance of 2.31 Å, as can be seen from Figure 2a. The water adsorption energies were calculated by subtracting the energies of the optimized water molecule and adsorbent bare slab ($E_{surface}$), from the optimized water-slab complex (surface@H₂O), using the equation

$$\Delta E_{ad} = E_{surface@H_2O} - (E_{H_2O} + E_{surface}) \qquad (2)$$

The smaller interatomic distance between water (O atoms of H₂O) and NiOOH (Ni of NiOOH) can lead to adsorption energy of −48 kcal/mol, as listed in Table 1. This strong interaction is responsible for the dissociation of water molecules. This finding has good correlation with the already reported work.[18,27]

We systematically doped NiOOH with an equal amount of Fe and Co atoms (from 3 to 16%), and their model optimized structures along with water molecules are given in Figure 2.
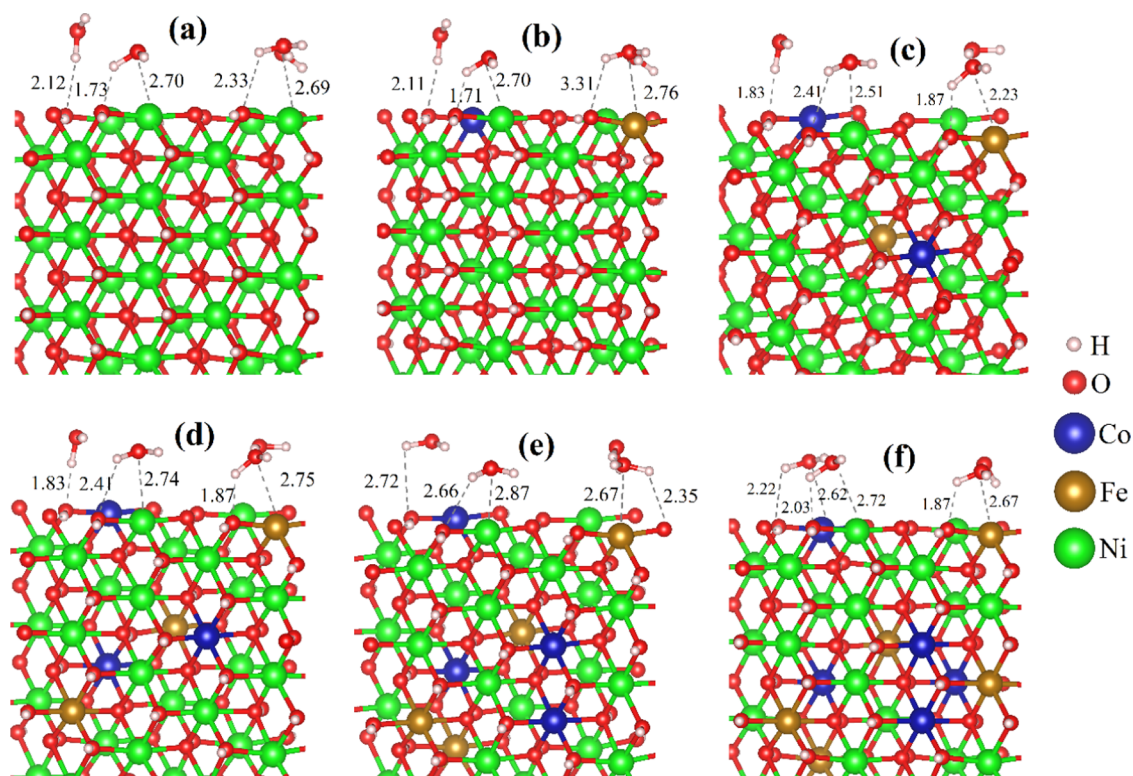
Figure 2. Optimized structures of (a) NiOOH@H_2O, (b) Ni$_{94\%}$Fe$_{3\%}$Co$_{3\%}$OOH@H_2O, (c) Ni$_{88\%}$Fe$_{6\%}$Co$_{6\%}$OOH@H_2O, (d) Ni$_{82\%}$Fe$_{9\%}$Co$_{9\%}$OOH@H_2O, (e) Ni$_{76\%}$Fe$_{12\%}$Co$_{12\%}$OOH@H_2O, and (f) Ni$_{68\%}$Fe$_{16\%}$Co$_{16\%}$OOH@H_2O system.

Table 1. Calculated Fermi Energy Level, VB, CB, Band Gap (vs Vacuum and Spin-Up States Only in a Unit of eV), Surface Formation Energies (eV/Å^2), Adsorption Energy E_{ad} (kcal/mol) of per Water Molecule Over the [010] Terminated Surface of NiOOH and Its Fe- and Co-Doped Species[a]

species	Fermi energy	VB	CB	m_e^*/m_0 (m_e)	m_h^*/m_0 (m_e)	band gap (eV)	formation energy	E_{ad}
NiOOH	−6.40	1.05	4.76	0.69	2.26	3.71	0.60	
NiOOH@H_2O	−6.49	1.11	4.49	0.68	2.20	3.38		−48
Ni$_{94\%}$Fe$_{3\%}$Co$_{3\%}$OOH	−6.36	1.08	4.75	0.70	2.25	3.67	0.61	
Ni$_{94\%}$Fe$_{3\%}$Co$_{3\%}$OOH@H_2O	−4.74	1	3.79	0.70	4.22	2.79		−38
Ni$_{88\%}$Fe$_{6\%}$Co$_{6\%}$OOH	−6.45	0.86	4.17	0.65	3.16	3.31	0.63	
Ni$_{88\%}$Fe$_{6\%}$Co$_{6\%}$OOH@H_2O	−5.68	1.00	3.69	0.74	7.83	2.69		−62
Ni$_{82\%}$Fe$_{9\%}$Co$_{9\%}$OOH	−5.67	0.99	4.28	0.66	6.06	3.27	0.69	
Ni$_{82\%}$Fe$_{9\%}$Co$_{9\%}$OOH@H_2O	−5.70	0.99	3.69	0.75	8.70	2.70		−54
Ni$_{76\%}$Fe$_{12\%}$Co$_{12\%}$OOH	−5.65	0.95	4.15	0.70	7.51	3.20	0.67	
Ni$_{76}$Fe$_{12}$Co$_{12}$OOH@H_2O	−6.45	0.82	4.24	0.70	3.85	3.42		−36
Ni$_{68\%}$Fe$_{16\%}$Co$_{16\%}$OOH	−5.69	0.89	4.19	0.70	8.62	3.30	0.68	
Ni$_{68\%}$Fe$_{16\%}$Co$_{16\%}$OOH@H_2O	−6.47	0.71	4.23	0.69	7.84	3.52		−32

[a]Effective masses of photogenerated electrons and holes are estimated from the calculated band structure along a suitable direction.

The surface formation energy of 3% Fe- and 3% Co-doped NiOOH (Ni$_{94\%}$Fe$_{3\%}$Co$_{3\%}$OOH) is 0.61 eV/Å^2, which is 0.01 eV/Å^2 higher than that of undoped NiOOH. So, with the incorporation of 3% Fe and 3% Co atoms, the stability of NiOOH increased, which is also consistent with the previous results.[28] However, the interaction energy of water molecules with Ni$_{94\%}$Fe$_{3\%}$Co$_{3\%}$OOH is lower (−38 kcal/mol) than that of the pristine surface, as can be seen from Figure 2b and Table 1. Moreover, the average interbond distance between the atoms of water and surface atoms of Ni$_{94\%}$Fe$_{3\%}$Co$_{3\%}$OOH is about 2.52 Å. In the case of the Ni$_{88\%}$Fe$_{6\%}$Co$_{6\%}$NiOOH@H_2O system, the absolute adsorption energy per water molecule is about −62 kcal/mol, which is higher than that of pristine NiOOH@H_2O and Ni$_{94\%}$Fe$_{3\%}$Co$_{3\%}$OOH@H_2O systems. The

reason behind this is that the proper amount of Co and Fe atoms as dopant is responsible for higher stability and reactivity. The relaxed crystal structure of Ni$_{88\%}$Fe$_{6\%}$Co$_{6\%}$OOH@H_2O is shown in Figure 2c, where the geometry does not change upon the incorporation of these atoms. So an equal amount of Co and Fe can easily replace Ni and does not distort the parental geometry of NiOOH. The surface stability of Ni$_{88\%}$Fe$_{6\%}$Co$_{6\%}$OOH is 0.63 eV/Å^2, as can be seen from Table 1.

Furthermore, we increased the doping amount of Fe and Co up to 16% such as Ni$_{82\%}$Fe$_{9\%}$Co$_{9\%}$OOH, Ni$_{76\%}$Fe$_{12\%}$Co$_{12\%}$OOH, and Ni$_{68\%}$Fe$_{16\%}$Co$_{16\%}$OOH, and their results are given in Table 1 and Figure 2. To determine the stability and successful interaction of water molecules,

electrostatic potential maps of all of these species are simulated. The electrostatic potential maps of $Ni_{88\%}Fe_{6\%}Co_{6\%}OOH$ and its water interacted system are given in Figure 3, while that of the remaining systems is shown in Figures S1−S4 of the Supporting Information.
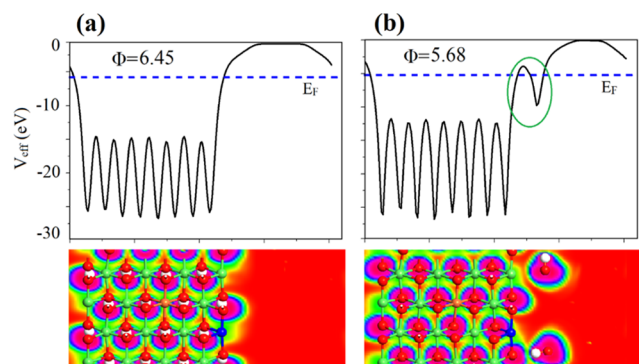

Figure 3. Averaged electrostatic potential map of $Ni_{88\%}Fe_{6\%}Co_{6\%}OOH$ (a) and $Ni_{88\%}Fe_{6\%}Co_{6\%}OOH@H_2O$ (b) along the Z-direction.

In the case of the $Ni_{82\%}Fe_{9\%}Co_{9\%}OOH$ system, the surface stability is 0.69 eV/Å^2, which is higher than that of $Ni_{88\%}Fe_{6\%}Co_{6\%}OOH$ and support the 9% doping of Fe and 9% Co atoms. However, the water adsorption energy is lower (−54 kcal/mol), which is responsible for higher oxygen overpotential. The stability of remaining catalyst models such as $Ni_{76\%}Fe_{12\%}Co_{12\%}OOH$ and $Ni_{68\%}Fe_{16\%}Co_{16\%}OOH$ are 0.67 and 0.68 eV/Å^2, while their per water molecule adsorption energies are −36 and −32 kcal/mol, respectively. The average interbond distance between the water molecules and the catalyst surface of NiOOH, $Ni_{94\%}Fe_{3\%}Co_{3\%}OOH$, $Ni_{88\%}Fe_{6\%}Co_{6\%}OOH$, $Ni_{82\%}Fe_{9\%}Co_{9\%}OOH$, $Ni_{76\%}Fe_{12\%}Co_{12\%}OOH$, and $Ni_{68\%}Fe_{16\%}Co_{16\%}OOH$ are 2.31, 2.52, 2.17, 2.32, 2.65, and 2.35 Å, respectively. The simulated surface formation energy and electrostatic potential maps of all of these species equally predict their feasibility. However, the per water molecule adsorption energy initially increases up to 6% Fe and 6% Co doping and then decreases along with the increase of these doping agents, as can be seen from Table 1. So, mild doping of NiOOH with an equal amount of Fe and Co atoms can significantly enhance the OER.

In addition, the higher the absolute water adsorption energy, the higher the catalytic activity and the lower the oxygen overpotential will be. Among all of these catalysts, $Ni_{88\%}Fe_{6\%}Co_{6\%}OOH$ has the highest absolute water adsorption energy, where the average interbond distance of water with the surface is also minimum. So, these dopants increase the overall charge density of Ni atoms, which consequently boost the OER activity (vide infra). In summary, the addition of 6% Fe and 6% Co dopants to pristine NiOOH is expected to improve both the stability and the catalytic activity of $Ni_{88\%}Fe_{6\%}Co_{6\%}OOH$ OER catalysts, through increased surface formation energies and water adsorption energies, respectively. The synergistic effect of 6% Fe and 6% Co dopants produces a greater effect, resulting in a formation energy of 0.63 eV/Å^2 and water adsorption energy of −62 kcal/mol.

2.2. Electronic Properties. The conduction band (CB) and valance band (VB) edge positions along with proper band gap are crucial for overall water electrolysis. In the case of OER catalysts, the VB must be well below the redox potential of water (~−5.80 eV at vacuum level), to efficiently oxidize water. The CB, VB, and band gap values of bulk NiOOH are simulated from the projected density of states (PDOS), as given in Figure 4.
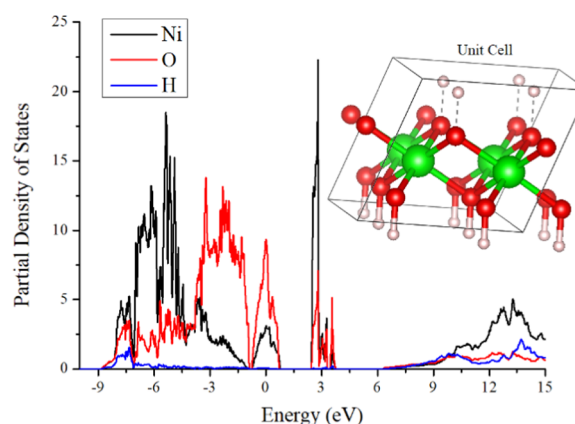

Figure 4. PDOS of NiOOH bulk; Fermi energy is set to zero.

The VB of NiOOH is composed of hybridized bonding orbitals of O and Ni atoms; however, the 2p orbitals of O are dominant as can be seen from Figure S5. On the other hand, the CB is constituted from the hybridized antibonding orbitals of Ni and O, where Ni 3d orbitals are dominant.

The band structure and PDOS of all of these species are simulated to find out the effect of dopants and water interaction on the resultant band gap and edge positions of NiOOH and its doped species. The PDOS and band structure (spin up only) of NiOOH are shown in Figure 5, where VB is composed of O 2p bonding orbitals and Ni 3d antibonding orbitals constitute the CB. The surface of NiOOH has a narrow band gap of 3.71 eV, where the VB and CB result in holes and electrons with effective masses of 2.26 and 0.69 m_e (see Table 1), respectively. Upon interaction with water, the overall band gap decreases from 3.71 to 3.38 eV, and water constitutes the bottom level of VB (Figure 5d).

The incorporation of Fe and Co atoms has significantly changed the electronic properties of pristine NiOOH, as can be seen from Table 1, Figures 6, and S6−S9 of the Supporting Information. The Fermi energy of all of these species changes, upon interaction with water, as can be seen from Table 1. The 3% Fe- and 3% Co-doped NiOOH such as $Ni_{94\%}Fe_{3\%}Co_{3\%}OOH$ has a similar band gap (3.67 eV) compared to the pristine species, but the effective masses of their charge carriers are heavier. Moreover, the adsorption energy of water is −38 kcal/mol, which is also lower than that of pristine NiOOH. It means that 3% doping of Fe and 3% Co atoms lower down the electronic properties of $Ni_{94\%}Fe_{3\%}Co_{3\%}OOH$. The effect of 6% Fe and 6% Co doping on NiOOH ($Ni_{88\%}Fe_{6\%}Co_{6\%}OOH$) is crucial as can be seen from its small band gap (3.31 eV), lighter effective masses of electrons (0.65 m_e) and holes (3.16 m_e), and decrease in Fermi energy level (−6.45 eV). This narrow band gap is due to extra bands, raised from the hybridized orbitals of Co and O atoms that occupy the CB and VB, see Figure 6.

Furthermore, the crystal structure of $Ni_{88\%}Fe_{6\%}Co_{6\%}OOH$ remains constant; however, its electronic properties such as band gap and effective masses of charge carriers are significantly improved. Its band gap reduces to 3.31 eV, while Fe and Co produce some flat bands in its band structure,
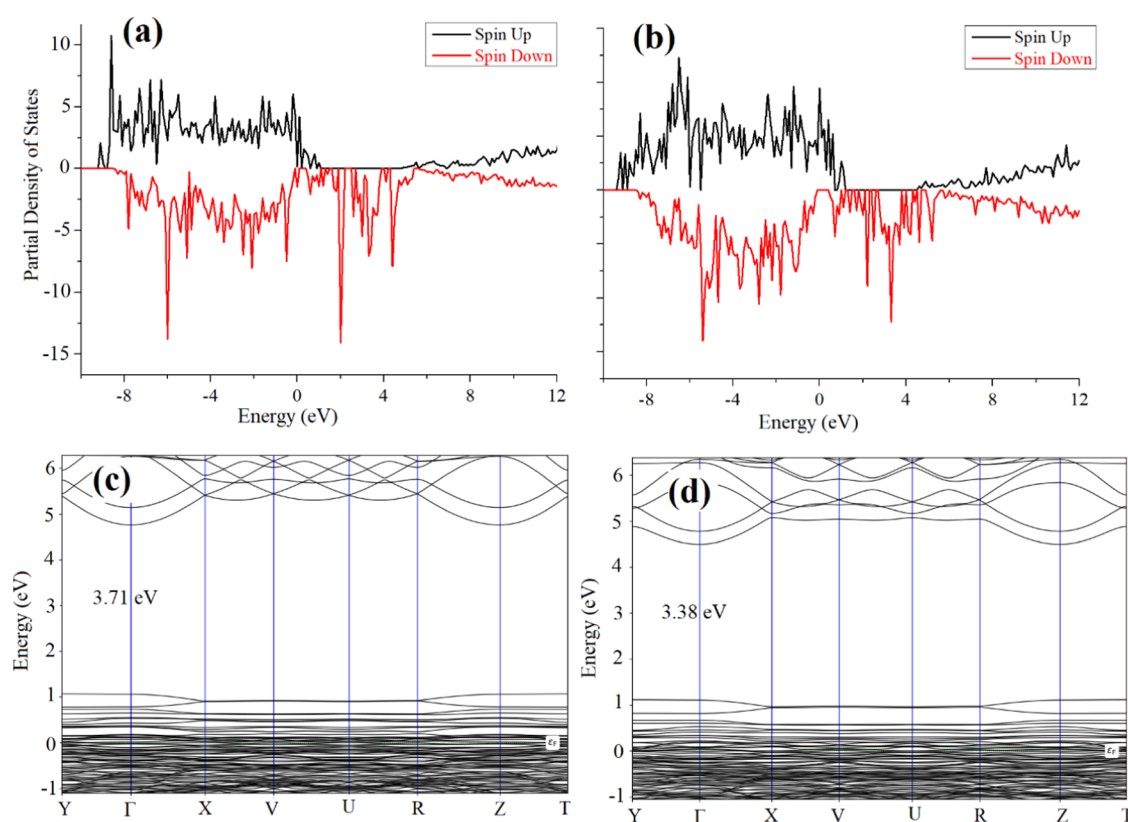
Figure 5. PDOS (spin up and down) of (a) NiOOH and (b) NiOOH@H$_2$O along with their band structures (spin up only) of (c) NiOOH and (d) NiOOH@H$_2$O.

as can be seen from Figure 6. These flat bands near the VB are responsible for stationary charge carriers (heavy mass of hole), which increase the difference between electron and hole, resulting in separation of charge carriers. Upon interaction with water molecules, the band gap of Ni$_{88\%}$Fe$_{6\%}$Co$_{6\%}$OOH@H$_2$O reduces to 2.69 eV, which predicts that H$_2$O molecules are dissociated into its constituents. So, the holes at VB can easily oxidize water upon external bias and consequently enhance the OER efficiency of the catalyst (vide infra).

A similar but less prominent situation is observed in the case of the Ni$_{82\%}$Fe$_{9\%}$Co$_{9\%}$OOH system as can be seen from Table 1. With the increase in the doping amount of Fe and Co above 9%, the band gap of resulting catalysts increases, which led us to predict those water molecules are not dissociated. Instead, water may exist in the form of stable molecules. These statements also corroborate and confirm the lower adsorption interaction of these species. Comparative analysis of the data of Table 1 led us to conclude that the VB energy level of all of the pristine NiOOH, Ni$_{94\%}$Fe$_{3\%}$Co$_{3\%}$OOH, and Ni$_{88\%}$Fe$_{6\%}$Co$_{6\%}$OOH systems are well below the redox potential of water ($\sim$−5.80 eV vs vacuum) and can easily perform the OER. On the other hand, VB of 9, 12, and 16% Fe- and Co-doped species are not below the redox potential of water, so high overpotential is required for the OER.

The charge analysis of all doped species is simulated from electron density difference (EDD), and their comparative two-dimensional (2D) EDD plots along the Z-direction are given in Figures 7 and S10−S13 of the Supporting Information. In Figure 7, the green- and blue-shaded areas represent charge accumulation and depletion, respectively. It can be observed that Fe and Co atoms have nicely shared their electronic cloud density with the host atom Ni and confirm the successful incorporation of these doping agents in NiOOH. Moreover, this type of charge sharing results in a strong hybridization among the orbitals of Ni, Fe, and Co atoms, which consequently improves the stability and catalytic activity in terms of more active sites (Ni, Fe, and Co).

3. CONCLUSIONS

Comprehensive DFT simulations have been carried out to investigate an efficient and highly stable Ni-based electrocatalyst for the OER in alkaline media. Initially, the β-NiOOH crystal structure was used as a primary simulating model for the Fe and Co dopants. A range of Fe and Co atoms (%) are employed as doping agents to increase the overall catalytic ability and stability of NiOOH. Our simulations indicate that mild doping of β-NiOOH (6% Fe and 6% Co atoms) increase surface formation energy, water adsorption energy, and change band gap and are therefore expected to improve catalyst stability, activity, and electronic properties, respectively. Moreover, Ni$_{88\%}$Fe$_{6\%}$Co$_{6\%}$OOH is stable and provides more catalytic sites at the surface of resulting catalysts for water adsorption and dissociation, which facilitate the OER. Besides, the Fe and Co dopants were found to play an important role in the resulting catalyst, by serving as catalytic sites for water adsorption and dissociation, making it stable and facilitating the OER. Finally, we propose that our theoretical procedure may provide guidelines for the design of other promising OER electrocatalysts.
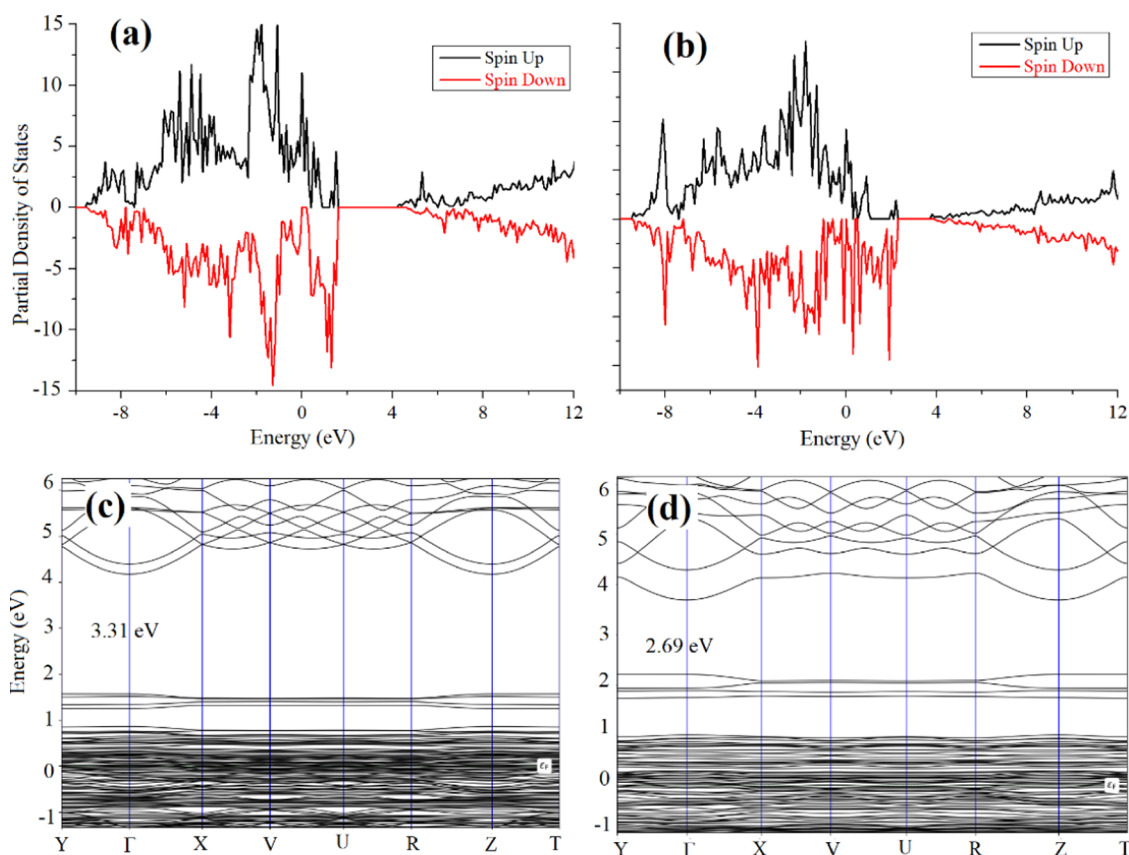
Figure 6. PDOS (spin up and down) of (a) $Ni_{88\%}Fe_{6\%}Co_{6\%}OOH$ and (b) $Ni_{88\%}Fe_{6\%}Co_{6\%}OOH@H_2O$, along with their band structures (spin up only) of (c) $Ni_{88\%}Fe_{6\%}Co_{6\%}OOH$ and (d) $Ni_{88\%}Fe_{6\%}Co_{6\%}OOH@H_2O$.
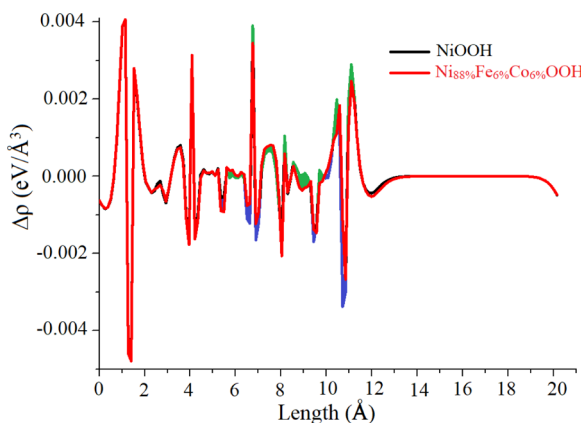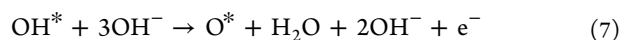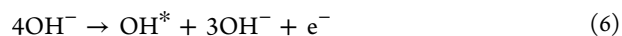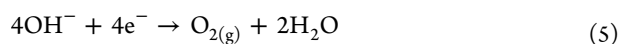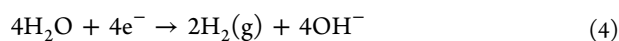

Figure 7. Average electron density difference ($\Delta\rho$) along the Z-direction for $Ni_{88\%}Fe_{6\%}Co_{6\%}OOH$ (red line) along with pristine NiOOH (black line). The green- and blue-shaded areas indicate electron accumulation and donation, respectively.

4. COMPUTATIONAL METHODOLOGY

The overall cell reaction of a water electrolyzer is expressed in eq 3. In alkaline media, the corresponding cathode and anode reactions are shown in eqs 4 and 5, respectively.

$$2H_2O \rightarrow 2H_{2(g)} + O_{2(g)} \tag{3}$$

$$4H_2O + 4e^- \rightarrow 2H_{2(g)} + 4OH^- \tag{4}$$

$$4OH^- + 4e^- \rightarrow O_{2(g)} + 2H_2O \tag{5}$$

$$4OH^- \rightarrow OH^* + 3OH^- + e^- \tag{6}$$

$$OH^* + 3OH^- \rightarrow O^* + H_2O + 2OH^- + e^- \tag{7}$$

$$O^* + H_2O + 2OH^- \rightarrow OOH^* + H_2O + OH^- + e^- \tag{8}$$

$$OOH^* + H_2O + OH^- \rightarrow O_{2(g)} + 2H_2O + e^- \tag{9}$$
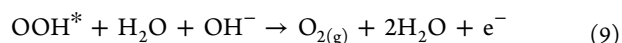
For the OER at the anode, generally, there are four steps involved as shown in reactions 6−9, where reaction 6 is the rate-determining step.[29,30] So, if the OH* adsorption energy is stronger at the surface of the proposed catalyst, then it means the overpotential will be lower.[30]

The oxygen overpotential can also be predicted from the adsorption of water molecules over the surface of the catalyst. The stronger the water molecule interaction is, the lower the oxygen overpotential will be.[31,32] Periodic DFT calculations have been performed on Quantum-ATK,[33] and the results are visualized on Virtual NanoLab Version 2019.12.[33] Both Ni and Fe have ferromagnetic behavior, so the SGGA + U method is employed that can accurately reproduce their electronic properties, especially band structure, etc. Thus, for the band-structure calculations, the U value is set to accurately represent the experimental data. Different Hubbard parameters are employed, where the $(U − J)$ value is selected for Ni. Recently, a U value of 4 eV has been reported by Toroker and co-worker,[34] 5.5 eV by Selloni et al.,[35] and 6.6 eV by Nørskov et al.[36] To fit the experimental data, these high $(U − J)$ values are required.[18] As explained previously, the β-NiOOH is highly stable among the various NiOOH phases. Its space group is

$P3m1$ (brucite),[20] and lattice parameters are $a = b = 3.12$ Å and $c = 4.66$ Å. After optimizing the lattice parameters of the bulk unit cell, a supercell $(2 \times 2 \times 2)$ is constructed, from which different low-index phases such as (001), (101), (100), and (010) NiOOH are built, as shown in Figure S14. The stability of these different slabs is confirmed from their positive surface formation energy and electrostatic potential. A range of the equal amount of Fe and Co atoms (%) are employed as doping agents to the most stable and efficient phase of NiOOH. Generalized gradient approximation (GGA) with the Perdew−Burke−Ernzerhof (PBE) exchange−correlation functional and pseudopotential of Hartwigsen Goedecker−Hutter (HGH) with tier 4 basis is employed for the structural and energy optimization, due to its superiority over other pseudopotentials.[37] In this work, we used a linear combination of atomic orbitals (LCAO) for Ni, Fe, Co, H, and O atoms.[38] A $5 \times 5 \times 5$ Monkhorst−Pack k-grid with an energy cutoff of 1500 eV is used for the unit cell, while a $5 \times 5 \times 1$ k-point mesh is used for the slabs. High-energy cutoff of 1500 eV is employed due to the LCAO calculator. In this calculator, one sets real-space density mesh cutoff, which is of an order of 70−200 Ha (2000−5000 eV) to that of the plane wave (PW) calculator. The density of states (DOS), partial density of states (PDOS), band structure, effective potential, electron density difference (EDD), and electron localization functional (ELF) calculations are performed with spin-polarized SGGA + U, where U values of 5 and 5.5 eV are selected for Ni and Fe atoms, respectively. The spin-polarized GGA + U method has been used due to the ferromagnetic nature of Fe and Ni. Moreover, this method can accurately reproduce the experimental values of Ni, Fe, and other related materials.

ASSOCIATED CONTENT

ⓈI Supporting Information

The Supporting Information is available free of charge at https://pubs.acs.org/doi/10.1021/acsomega.0c02679.

> Optimized geometric structures, electrostatic potential maps, PDOS, band structures, electron density difference, and cohesive and surface formation energies of NiOOH and its doped species (PDF)

AUTHOR INFORMATION

Corresponding Author

Xiaohong Li − Renewable Energy Group, College of Engineering, Mathematics and Physical Sciences, University of Exeter, Penryn, Cornwall TR10 9FE, United Kingdom; ⓞ orcid.org/0000-0003-4450-4617; Phone: +44 1326 25 5769; Email: X.Li@exeter.ac.uk

Authors

Habib Ullah − Renewable Energy Group, College of Engineering, Mathematics and Physical Sciences, University of Exeter, Penryn, Cornwall TR10 9FE, United Kingdom; ⓞ orcid.org/0000-0001-9290-0265

Adeline Loh − Renewable Energy Group, College of Engineering, Mathematics and Physical Sciences, University of Exeter, Penryn, Cornwall TR10 9FE, United Kingdom

David P. Trudgeon − Renewable Energy Group, College of Engineering, Mathematics and Physical Sciences, University of Exeter, Penryn, Cornwall TR10 9FE, United Kingdom

Complete contact information is available at:
https://pubs.acs.org/10.1021/acsomega.0c02679

Notes

REFERENCES

(1) Wang, X. P.; Wu, H.; Xi, S.; Lee, W.; Zhang, J.; Wu, Z.; Wang, J.; Hu, T.; Liu, L.; Han, Y.; et al. Strain Stabilized Nickel Hydroxide Nanoribbons for Efficient Water Splitting. Energy Environ. Sci. 2020, 13, 229−237.

(2) Gupta, S.; Patel, M. K.; Miotello, A.; Patel, N. Metal Boride-Based Catalysts for Electrochemical Water-Splitting: A Review. Adv. Funct. Mater. 2020, 30, No. 1906481.

(3) Seitz, L. C.; Dickens, C. F.; Nishio, K.; Hikita, Y.; Montoya, J.; Doyle, A.; Kirk, C.; Vojvodic, A.; Hwang, H. Y.; Norskov, J. K.; et al. A Highly Active and Stable $IrO_x/SrIrO_3$ Catalyst for the Oxygen Evolution Reaction. Science 2016, 353, 1011−1014.

(4) Sun, Y.; Lee, H.-W.; Seh, Z. W.; Liu, N.; Sun, J.; Li, Y.; Cui, Y. High-Capacity Battery Cathode Prelithiation to Offset Initial Lithium Loss. Nat. Energy 2016, 1, No. 15008.

(5) Seitz, L. C.; Hersbach, T. J.; Nordlund, D.; Jaramillo, T. F. Enhancement Effect of Noble Metals on Manganese Oxide for the Oxygen Evolution Reaction. J. Phys. Chem. Lett. 2015, 6, 4178−4183.

(6) Reier, T.; Oezaslan, M.; Strasser, P. Electrocatalytic Oxygen Evolution Reaction (OER) on Ru, Ir, and Pt Catalysts: A Comparative Study of Nanoparticles and Bulk Materials. ACS Catal. 2012, 2, 1765−1772.

(7) Mamaca, N.; Mayousse, E.; Arrii-Clacens, S.; Napporn, T.; Servat, K.; Guillet, N.; Kokoh, K. Electrochemical Activity of Ruthenium and Iridium Based Catalysts for Oxygen Evolution Reaction. Appl. Catal., B 2012, 111, 376−380.

(8) Burke, M. S.; Enman, L. J.; Batchellor, A. S.; Zou, S.; Boettcher, S. W. Oxygen Evolution Reaction Electrocatalysis on Transition Metal Oxides and (Oxy) Hydroxides: Activity Trends and Design Principles. Chem. Mater. 2015, 27, 7549−7558.

(9) Song, F.; Bai, L.; Moysiadou, A.; Lee, S.; Hu, C.; Liardet, L.; Hu, X. Transition Metal Oxides as Electrocatalysts for the Oxygen Evolution Reaction in Alkaline Solutions: An Application-Inspired Renaissance. J. Am. Chem. Soc. 2018, 140, 7748−7759.

(10) Patil, U.; Gurav, K.; Fulari, V.; Lokhande, C.; Joo, O. S. Characterization of Honeycomb-like "β-Ni(OH)$_2$" Thin Films Synthesized by Chemical Bath Deposition Method and their Supercapacitor Application. J. Power Sources 2009, 188, 338−342.

(11) Barton, R. T.; Mitchell, P.; Hampson, N. The Electro-technology of the Nickel Positive Electrode: A Review of the Recent Literature. Surf. Coat. Technol. 1986, 28, 1−9.

(12) Corrigan, D. A. The Catalysis of the Oxygen Evolution Reaction by Iron Impurities in Thin Film Nickel Oxide Electrodes. J. Electrochem. Soc. 1987, 134, 377−384.

(13) Chakthranont, P.; Kibsgaard, J.; Gallo, A.; Park, J.; Mitani, M.; Sokaras, D.; Kroll, T.; Sinclair, R.; Mogensen, M. B.; Jaramillo, T. F. Effects of Gold Substrates on the Intrinsic and Extrinsic Activity of High-Loading Nickel-Based Oxyhydroxide Oxygen Evolution Catalysts. ACS Catal. 2017, 7, 5399−5409.

(14) Swesi, A. T.; Masud, J.; Nath, M. Nickel Selenide as a High-Efficiency Catalyst for Oxygen Evolution Reaction. Energy Environ. Sci. 2016, 9, 1771−1782.

(15) Li, Y.-F.; Selloni, A. Mechanism and Activity of Water Oxidation on Selected Surfaces of Pure and Fe-Doped NiO_x. ACS Catal. 2014, 4, 1148−1153.

(16) Huang, L.-a.; He, Z.; Guo, J.; Pei, S.-e.; Shao, H.; Wang, J. Photodeposition Fabrication of Hierarchical Layered Co-Doped Ni Oxyhydroxide ($Ni_xCo_{1−x}OOH$) Catalysts with Enhanced Electrocatalytic Performance for Oxygen Evolution Reaction. Nano Res. 2020, 13, 246−254.

(17) Bode, H.; Dehmelt, K.; Witte, J. Zur Kenntnis Der Nickelhydroxidelektrode—I. Über Das Nickel (II)-Hydroxidhydrat. *Electrochim. Acta* **1966**, *11*, 1079−1087.

(18) Tkalych, A. J.; Yu, K.; Carter, E. A. Structural and Electronic Features of β-Ni (OH)$_2$ and β-NiOOH from First Principles. *J. Phys. Chem. C* **2015**, *119*, 24315−24322.

(19) Young, K.-H.; Wang, L.; Yan, S.; Liao, X.; Meng, T.; Shen, H.; Mays, W. Fabrications of High-Capacity Alpha-Ni(OH)$_2$. *Batteries* **2017**, *3*, No. 6.

(20) Casas-Cabanas, M.; Canales-Vázquez, J.; Rodríguez-Carvajal, J.; Palacín, M. R. Deciphering the Structural Transformations During Nickel Oxyhydroxide Electrode Operation. *J. Am. Chem. Soc.* **2007**, *129*, 5840−5842.

(21) Ullah, H.; Tahir, A. A.; Bibi, S.; Mallick, T. K.; Karazhanov, S. Z. Electronic Properties of β-TaON and its Surfaces for Solar Water Splitting. *Appl. Catal., B* **2018**, *229*, 24−31.

(22) Ullah, H.; Tahir, A. A.; Mallick, T. K. Structural and Electronic Properties of Oxygen Defective and Se-doped p-type BiVO$_4$(001) Thin Film for the Applications of Photocatalysis. *Appl. Catal., B* **2018**, *224*, 895−903.

(23) Kittel, C. *Introduction to Solid State Physics*, 8th ed.; Wiley: New York, 1996; pp 1−675.

(24) Nasir, S. N. F. M.; Ullah, H.; Ebadi, M.; Tahir, A. A.; Sagu, J. S.; Mat Teridi, M. A. New Insights into Se/BiVO$_4$ Heterostructure for Photoelectrochemical Water Splitting: A Combined Experimental and DFT Study. *J. Phys. Chem. C* **2017**, *121*, 6218−6228.

(25) Mohamed, N. A.; Ullah, H.; Safaei, J.; Ismail, A. F.; Mohamad Noh, M. F.; Soh, M. F.; Ibrahim, M. A.; Ludin, N. A.; Mat Teridi, M. A. Efficient Photoelectrochemical Performance of γ-Irradiated g-C$_3$N$_4$ and its g-C$_3$N$_4$@ BiVO$_4$ Heterojunction for Solar Water Splitting. *J. Phys. Chem. C* **2019**, *123*, 9013−9026.

(26) Safaei, J.; Ullah, H.; Mohamed, N. A.; Noh, M. F. M.; Soh, M. F.; Tahir, A. A.; Ludin, N. A.; Ibrahim, M. A.; Isahak, W. N. R. W.; Teridi, M. A. M. Enhanced Photoelectrochemical Performance of Z-scheme g-C$_3$N$_4$/BiVO$_4$ Photocatalyst. *Appl. Catal., B* **2018**, *234*, 296−310.

(27) Wang, H. Y.; Hsu, Y. Y.; Chen, R.; Chan, T. S.; Chen, H. M.; Liu, B. Ni^{3+}-Induced Formation of Active NiOOH on the Spinel Ni−Co Oxide Surface for Efficient Oxygen Evolution Reaction. *Adv. Energy Mater.* **2015**, *5*, No. 1500091.

(28) Conesa, J. C. Electronic Structure of the (Undoped and Fe-doped) NiOOH O$_2$ Evolution Electrocatalyst. *J. Phys. Chem. C* **2016**, *120*, 18999−19010.

(29) Zhang, J.; Zhao, Z.; Xia, Z.; Dai, L. A Metal-Free Bifunctional Electrocatalyst for Oxygen Reduction and Oxygen Evolution Reactions. *Nat. Nanotechnol.* **2015**, *10*, 444.

(30) Kwon, N. H.; Kim, M.; Jin, X.; Lim, J.; Kim, I. Y.; Lee, N.-S.; Kim, H.; Hwang, S.-J. A Rational Method to Kinetically Control the Rate-Determining Step to Explore Efficient Electrocatalysts for the Oxygen Evolution Reaction. *NPG Asia Mater.* **2018**, *10*, 659−669.

(31) Jahangiri, S.; Mosey, N. J. Molecular Structure and Interactions of Water Intercalated in Nickel Hydroxide. *Phys. Chem. Chem. Phys.* **2018**, *20*, 11444−11453.

(32) Costanzo, F. Effect of Doping β-NiOOH with Co on the Catalytic Oxidation of Water: DFT+U Calculations. *Phys. Chem. Chem. Phys.* **2016**, *18*, 7490−7501.

(33) Smidstrup, S.; Markussen, T.; Vancraeyveld, P.; Wellendorff, J.; Schneider, J.; Gunst, T.; Verstichel, B.; Stradi, D.; Khomyakov, P. A.; Vej-Hansen, U. G. QuantumATK: An Integrated Platform of Electronic and Atomic-Scale Modelling Tools. *J. Phys.: Condens. Matter* **2019**, *32*, No. 015901.

(34) Zaffran, J.; Toroker, M. C. Metal−Oxygen Bond Ionicity as an Efficient Descriptor for Doped NiOOH Photocatalytic Activity. *Chem. Phys. Chem.* **2016**, *17*, 1630−1636.

(35) Li, Y.-F.; Selloni, A. Mosaic Texture and Double c-axis Periodicity of β-NiOOH: Insights from First-Principles and Genetic Algorithm Calculations. *J. Phys. Chem. Lett.* **2014**, *5*, 3981−3985.

(36) Friebel, D.; Louie, M. W.; Bajdich, M.; Sanwald, K. E.; Cai, Y.; Wise, A. M.; Cheng, M.-J.; Sokaras, D.; Weng, T.-C.; Alonso-Mori, R.; et al. Identification of Highly Active Fe Sites in (Ni, Fe)OOH for Electrocatalytic Water Splitting. *J. Am. Chem. Soc.* **2015**, *137*, 1305−1313.

(37) Enkovaara, J.; Rostgaard, C.; Mortensen, J. J.; Chen, J.; Dułak, M.; Ferrighi, L.; Gavnholt, J.; Glinsvad, C.; Haikola, V.; Hansen, H.; et al. Electronic Structure Calculations with GPAW: A Real-Space Implementation of the Projector Augmented-Wave Method. *J. Phys: Condens. Matter* **2010**, *22*, No. 253202.

(38) Kresse, G.; Joubert, D. From Ultrasoft Pseudopotentials to the Projector Augmented-Wave Method. *Phys. Rev. B* **1999**, *59*, 1758.